# Initial Orbit Determination from Ambiguous TDOA and FDOA Measurements of Passive Radio Frequency Signals

**Benjamin Feuge-Miller**
*Applied Research Laboratories, The University of Texas at Austin*
**Andrew Joplin**
*Applied Research Laboratories, The University of Texas at Austin*

**Johnathan York**
*Applied Research Laboratories, The University of Texas at Austin*

## ABSTRACT

Improved methods for independently detecting and monitoring spacecraft are vital for Space Domain Awareness given the rapidly increasing number of active satellites in Earth orbit. Beyond simply identifying new satellites or reacquiring tracks after loss of custody, independent monitoring can mitigate cross-tagging risks and improve confidences in conjunction assessments for collision avoidance. Passive radio frequency (RF) data can provide a powerful source of information for this task by identifying periodic signatures, even if the structure of such signals is not known a priori [7]. Compared to electro-optical measurements, RF signal data can be collected regardless of the illumination geometry and satellite material makeup. Furthermore, passive RF signals can be observed beyond the range of typical active radar sensors. However, many of the algorithms designed to detect and characterize unique signals from the broad RF spectrum suffer from significant ambiguities in resulting pseudo-range measurements due to the periodic nature of the signals. Traditional precision tracking algorithms (e.g., Kalman filters) and initial orbit determination techniques require external reference data to disambiguate these measurements. Employing such external data can prevent the data from being used to establish an independent estimate. In this paper, we propose an initial orbit determination algorithm designed to exploit ambiguous RF data from arbitrary signals, even when there is a complete lack of a priori information about the transmitter orbit.

To remove the unknown transmitter clock from the measurement model, state estimation is performed on time difference of arrival (TDOA) and frequency difference of arrival (FDOA) data from simultaneous pseudo-range and Doppler measurements of the RF signal. Given a lack of prior information, the algorithm begins by defining a coarse set of Keplerian state vectors across a range of altitudes. These initial guesses are assumed to be very poor, preventing linearization of the estimation problem. The proposed algorithm adopts a basin-hopping optimization technique with direct-search minimization following a three-stage approach, at first using only FDOA data and information about the receiver positions to drive convergence. We then refine the FDOA estimate by restricting the search space using a set of visibility constraints, and finally perform non-linear estimation using the full data set including ambiguous TDOA data, enabling us to locate the global minimum from among many local minima in a computationally tractable manner. To improve convergence on a wide range of orbits – spanning varied eccentricities, inclinations, and altitudes – we transform the Keplerian state vector to Poincaré orbital elements for optimization. The resulting initial orbit estimate can be used to disambiguate the measurement data and seed precision tracking algorithms independent of prior information.

We demonstrate the flexibility of this approach by simulating measurements from random IGS stations for a diverse set of example orbits, as may be done in a professional observation network. To validate our results, we also consider real measurements from these sites, focusing on available GNSS signal data provided through NASA's Crustal Dynamics Data Information System (CDDIS) archive with manually introduced ambiguities. The results from this study support the use of the presented initial orbit determination algorithm in leveraging ambiguous measurements of passive radio frequency signals for the independent detection, tracking, and characterization of active spacecraft, addressing significant challenges in the use of such measurement data.

# 1. INTRODUCTION

The increasingly crowded orbital environment requires significant expansions of object discovery and tracking capabilities to maintain safety and sustainability. In particular, fully independent detection and tracking systems should be established to identify new satellites, reacquire satellites in the event of cross-tagging or loss of custody (e.g., due to unexpected maneuvers), and improve state estimation for confident collision avoidance by integrating independent data.

Recent work has shown promise in discovering and characterizing so-called "signals of opportunity" from active spacecraft [7]. By blindly identifying unique signals from the broad spectrum of passive radio frequency (RF) data, transmitters can be independently found without any a priori information of the satellite state (i.e., published ephemerides). These signals can be detected at very long ranges, and can be collected irrespective of whether the satellite is optically visible due to illumination geometries and reflective satellite surfaces. Furthermore, the detection of a signal followed by subsequent orbit determination ties a trackable physical spacecraft to characteristic information about its active nature and transmitted frequency. These factors make passive RF signals particularly noteworthy for advancing Space Domain Awareness.

However, the process of detecting periodic signals can result in pseudo-range ambiguities which must be removed prior to most precision estimation and even initial orbit determination algorithms. If no assumptions about the transmitter orbit are made, disambiguation of the measurement data can be extremely difficult. We present an algorithm for initial orbit determination of passive RF signals assuming no prior information, producing state estimates which can be used to disambiguate the data and seed precision estimation techniques. We demonstrate the flexibility and robustness of our approach on simulated data from a global set of IGS stations, validating the results on selected real data.

# 2. BACKGROUND

## 2.1 Measurment Data

Consider a transmitting satellite $sv$ and two stationary receivers $rx_1$ and $rx_2$. At time $t$, the geometric range $\rho$ and range-rate $\dot{\rho}$ can be derived by comparing position and velocity state vectors $\mathbf{x}(t)$ and $\dot{\mathbf{x}}(t)$ between the transmitter and receiver. Our objective is to use observable measurements of the range and range-rate to estimate the initial orbit state $\mathbf{x}_{sv}(t_0)$.

$$\rho_i(t) = \|\mathbf{x}_{rx_i}(t) - \mathbf{x}_{sv}(t)\|_2 \tag{1a}$$

$$\dot{\rho}_i(t) = \frac{(\mathbf{x}_{rx_i}(t) - \mathbf{x}_{sv}(t))^T(\dot{\mathbf{x}}_{rx_i}(t) - \dot{\mathbf{x}}_{sv}(t))}{\|\mathbf{x}_{rx_i}(t) - \mathbf{x}_{sv}(t)\|_2} \tag{1b}$$

The pseudo-range $R_\rho$ (in meters) can be measured by differencing the times of transmission ($t_0$) and reception at either receiver ($t_1, t_2$). The model includes clock ($\delta t$), tropospheric and ionospheric delays ($\delta T$), and other effects and statistical uncertainties ($\varepsilon_t$) – let $c$ be the speed of light.

$$R_{\rho_i} = c(t_1 - t_0) \approx \rho_i + c(\delta t_{rx_i} - \delta t_{sv}) + \delta T_i + \varepsilon_t \tag{2}$$

For some signals $t_0$ and $\delta t_{sv}$ may be unknown. If a unique start to the transmitted signal can be identified at either receiver, the time difference of arrival (TDOA, $\Delta_T$, in seconds) can be used to cancel out these unknowns.

$$c\Delta_T = R_{\rho 1} - R_{\rho 2} = c(t_1 - t_2) \approx (\rho_1 - \rho_2) + c(\delta t_{rx1} - \delta t_{rx2}) + (\delta T_1 - \delta T_2 + \varepsilon_t) \tag{3}$$

In practice, the start of a transmitted signal may be unknown, and a periodic signal received by either observer may be measured at a different number of cycles. This results in a frequency-based ambiguity ($T_f$) acting as a modulus on the measurement (the " mod " operator).

$$c(\Delta_T \mod T_f) = c((t_1 - t_2) \mod T_f) \approx ((\rho_1 - \rho_2) + c(\delta t_{rx1} - \delta t_{rx2}) + (\delta T_1 - \delta T_2 + \varepsilon_t)) \mod (cT_f) \tag{4}$$

It is assumed that any change in the satellite position $\mathbf{x}_{sv}$ or drift in $\delta t_{sv}$ between the transmission time of either cycle is dominated by other model uncertainties in $\varepsilon_t$ and the orbit propagation model. These simplifying assumptions are not necessarily detrimental for coarse initial orbit determination, but errors should be mitigated in precision orbit determination following the initial estimate.

The Doppler shift $F_{\dot{\rho}}$ (in meters/second) can be measured by differencing the transmitted carrier frequency ($f_0$) and either received frequency ($f_1, f_2$). The model involves clock drift rates ($\dot{\delta} t$), drift in tropospheric and ionospheric delay ($\dot{\delta T}$), and other effects and uncertainties ($\dot{\varepsilon}_t$).

$$F_{\dot{\rho}} = \frac{c}{f_0}(f_1 - f_0) \approx \dot{\rho} + c(\dot{\delta}_{rx} - \dot{\delta}_{sv}) + \dot{\delta T} + \dot{\varepsilon}_t \tag{5}$$

For some signals $\dot{\delta} t_{sv}$ may be unknown, and the frequency difference of arrival (FDOA, $\Delta_F$, in hertz) is used to cancel out this unknown.

$$\frac{c}{f_0}\Delta_F = F_{\dot{\rho}1} - F_{\dot{\rho}2} = \frac{c}{f_0}(f_1 - f_2) \approx (\dot{\rho}_1 - \dot{\rho}_2) + c(\dot{\delta}_{rx1} - \dot{\delta}_{rx2}) + (\dot{\delta T}_1 - \dot{\delta T}_2 + \dot{\varepsilon}_t) \tag{6}$$

For the estimation model, we will assume that the environmental delays $\delta T$ and $\dot{\delta T}$ are again dominated by other model uncertainties and the orbit propagation model. Once we have estimated the satellite state, the unknown transmitter clock $\delta t_{sv}$ and drift $\dot{\delta} t_{sv}$ can be solved for separately.

### 2.2 Disambiguation

For this work, we assume the range measurements $\rho_{\text{meas.}}$ for evaluating the TDOA data have a $T_f$-second ambiguity known from observing the RF signal. Letting $N_f$ be the integer ambiguity corresponding to the number of $T_f$-second phase cycles, the relationship between the ambiguity and range measurement is straightforward.

$$\rho(t) = \rho_{\text{meas.}} + N_f \times (cT_f) \approx \|\mathbf{x}_{rx_i}(t) - \mathbf{x}_{sv}(t)\|_2 \tag{7}$$

If we know the transmitter state, we can disambiguate the range measurements through simple algebra, rounding normally to the nearest integer.

$$N_f = \text{round}\left(\frac{\|\mathbf{x}_{rx_i}(t) - \mathbf{x}_{sv}(t)\|_2 - \rho_{\text{measurement}}}{cT_f}\right) \tag{8}$$

However, in our application we assume no prior information about the transmitter, and must perform state estimation prior to disambiguating the measurement data. Note that for effective disambiguation the exact transmitter position need not be known, but only to an accuracy proportional to $cT_f$. For example, a sufficient upper bound for resolving a 1ms ambiguity would be a maximum TDOA measurement residual of 150km.

### 2.3 State Estimation

Given $N$ TDOA/FDOA measurements collected at various transmission times and receiver pairs $\{t_i, (rx_1^i, rx_2^i)\}_{i=1}^N$, the initial orbit state $\mathbf{x}_{sv}^* := \mathbf{x}_{sv}(t_*)$ must be propagated in time from a common initial epoch $t_*$ to each measurement epoch $t_i$. We will perform this transformation using the standard Simplified General Perturbations-4 (SGP4) propagator, including atmospheric drag [16].

$$\mathbf{x}_{sv}^* := \text{SGP4}(\mathbf{x}_{sv}(t_*), t_*, t_i) \tag{9}$$

The estimated state $\hat{\mathbf{x}}_{sv}^*$ is solved to minimize some residual function comparing the actual measurements $\{\Delta_T^i, \Delta_F^i\}_{i=1}^N$ to those estimated from the above models $\{\tilde{\Delta}_T^i(\mathbf{x}_{sv}^*), \tilde{\Delta}_F^i(\mathbf{x}_{sv}^*)\}_{i=1}^N$. We assume that the TDOA and FDOA measurements are independent and consider a cost function weighting time and frequency differently through $\sigma_{TDOA}$ and $\sigma_{FDOA}$ — these weights could include other considerations such as trustworthiness of each receiver pair, observability, and so on.

$$J_{TDOA}(\mathbf{x}_{sv}(t_0^*)) = \sum_{i=1}^{N} \sigma_{TDOA}^{-2}\left((\Delta_T^i - \tilde{\Delta}_T^i) \mod (cT_f)\right)^2 \tag{10a}$$

$$J_{FDAO}(\mathbf{x}_{sv}(t_0^*)) = \sum_{i=1}^{N} \sigma_{FDOA}^{-2}\left(\Delta_F^i - \tilde{\Delta}_F^i\right)^2 \tag{10b}$$

$$\hat{\mathbf{x}}_{sv}^* = \arg\min_{\mathbf{x}_{sv}(t_0^*)} \left(J_{TDOA}(\mathbf{x}_{sv}(t_0^*)) + J_{FDAO}(\mathbf{x}_{sv}(t_0^*))\right) \tag{11}$$

If a good initial state estimate is known and the measurements were non-ambiguous, many established techniques exist for precision orbit determination (OD) — e.g., Kalman filtering. However, we are concerned with blind initial orbit determination (IOD) having no a priori knowledge. Many batch least squares [13, 17] or minimum variance estimators [5, 2] classically used for IOD depend upon linearization of the measurement and dynamics models, thus requiring some reasonably accurate state estimate $\hat{\mathbf{x}}_{sv}^{*}$. Non-linear and probabilistic solvers such as Gaussian mixture filters [6, 14] typically also require reference trajectories for optimization, use other data such as electro-optical measurements to avoid uncertainties in RF measurements, and are frequently limited to select orbital cases. Beyond this concern with a priori knowledge, many OD and IOD methods concerned with TDOA data also ignore the inherent ambiguities involved with blindly detected periodic signals, and disambiguation is not possible until the state is estimated to reasonable accuracy [7]. This work attempts to address these concerns for enabling fully independent IOD using passive RF data including ambiguous measurements.

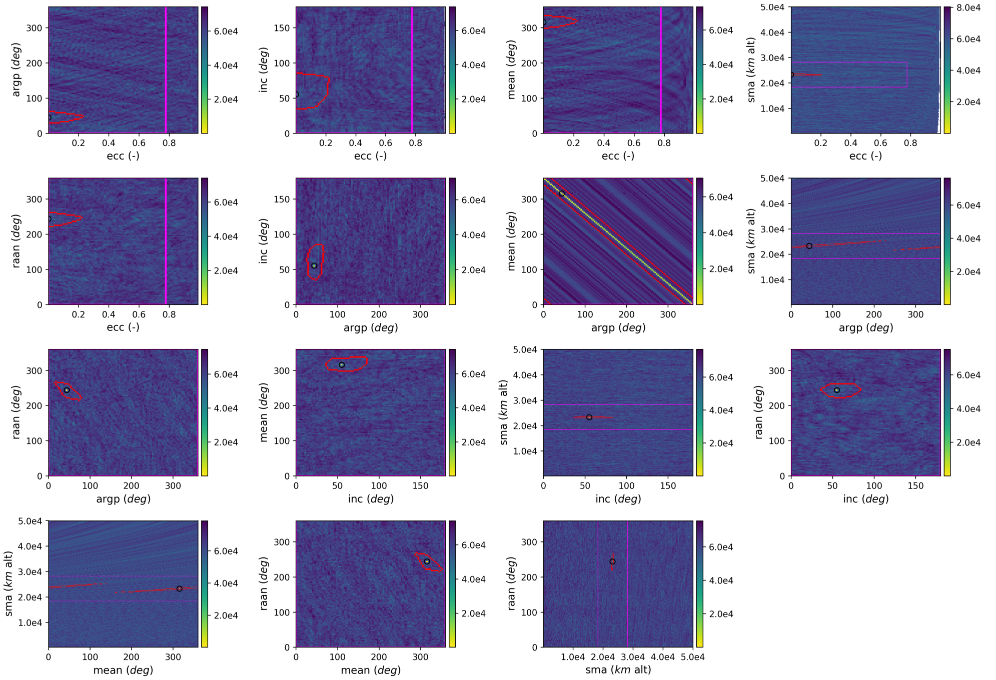

Fig. 1: Full TDOA+FDOA residual cost function evaluated over two-dimensional slices of the Keplerian state-space around truth for a simulated Galileo GNSS satellite (NORAD 40889, Section 3.3). Lower residual costs are shown in yellow with the true TLE state circled in black. The red borders denote states visible above the horizon at all measurements, and the pink borders denote altitude and eccentricity constraints (Section 3.1.2).

# 3. METHODS

## 3.1 Optimization

### 3.1.1 Poincaré Orbital Elements

The state vector describing the satellite position and velocity coordinates are typically described by an equivalent unique set of parameters defining the orbit characteristics. The classical Keplerian orbital elements include the semi-major axis ($a$), eccentricity ($e$), inclination ($i$), right ascension of the ascending node ($\Omega$), argument of perigee ($\omega$), and mean anomaly ($M$). However, these elements result in singularities for circular and/or equatorial orbits, and half of the elements suffer from phase wrapping concerns. It is therefore useful to transform the elements into an equivalent set with better behaviors. The transform will also prove convenient for bounding the search space of the solver, as will be discussed in Section 3.1.2.

The Delaunay elements describe the same vector in terms of canonical variables, conjugate coordinate-momenta pairs useful in describing the Hamiltonian dynamics of the system. The classical Delaunay elements consist of the conjugate pairs $(M, L)$, $(\omega, G)$, and $(\Omega, H)$ — where variable $G$ defines the angular momentum of the orbit [15].

$$L = \sqrt{\mu a}, \qquad G = L\sqrt{1-e^2}, \qquad H = G\cos i \tag{12}$$

The so-called modified Delaunay variables are derived in terms of the mean longitude $(\lambda)$ and longitude of periapsis $(\omega + \Omega)$. We will refer to these variables as the conjugate pairs $(\lambda, L)$, $(p, P)$, and $(q, Q)$[1, 8].

$$\lambda = M + \omega + \Omega, \qquad L = L \tag{13a}$$

$$p = -\omega - \Omega, \qquad P = L - G \tag{13b}$$

$$q = -\Omega, \qquad Q = G - H \tag{13c}$$

From this formulation we derive the Poincaré orbital elements, a set of canonical and equinoctial variables which are non-singular for circular and equatorial orbits (in either case, one of the conjugate pairs will go to zero). These elements will be referred to as $(\lambda, L)$, $(x_1, y_1)$, and $(x_2, y_2)$ to avoid confusion with the Delaunay variables.

$$x_1 = \sqrt{2P}\sin p, \qquad y_1 = \sqrt{2P}\cos p \tag{14a}$$

$$x_2 = \sqrt{2Q}\sin q, \qquad y_2 = \sqrt{2Q}\cos q \tag{14b}$$

The convenient properties of Poincaré elements mentioned above and with regards to bounding constraints discussed in Section 3.1.2 below make this space preferable to Keplerian elements. However, as the SGP4 model propagates Keplerian state vectors, we simply apply the forward and inverse transforms immediately before and after any necessary optimization steps. The inverse transform from Poincaré back to Keplerian elements is straightforward [4].

$$p = \tan^{-1}\frac{x_1}{y_1}, \qquad q = \tan^{-1}\frac{x_2}{y_2} \tag{15a}$$

$$P = \frac{1}{2}(x_1^2 + y_1^2), \qquad Q = \frac{1}{2}(x_2^2 + y_2^2) \tag{15b}$$

$$G = L - P, \qquad H = G - Q \tag{15c}$$

$$a = \frac{L^2}{\mu}, \qquad e = \sqrt{1 - \frac{G^2}{L^2}}, \qquad i = \cos^{-1}\frac{H}{G} \tag{15d}$$

$$\Omega = -q, \qquad \omega = q - p, \qquad M = \lambda + p \tag{15e}$$

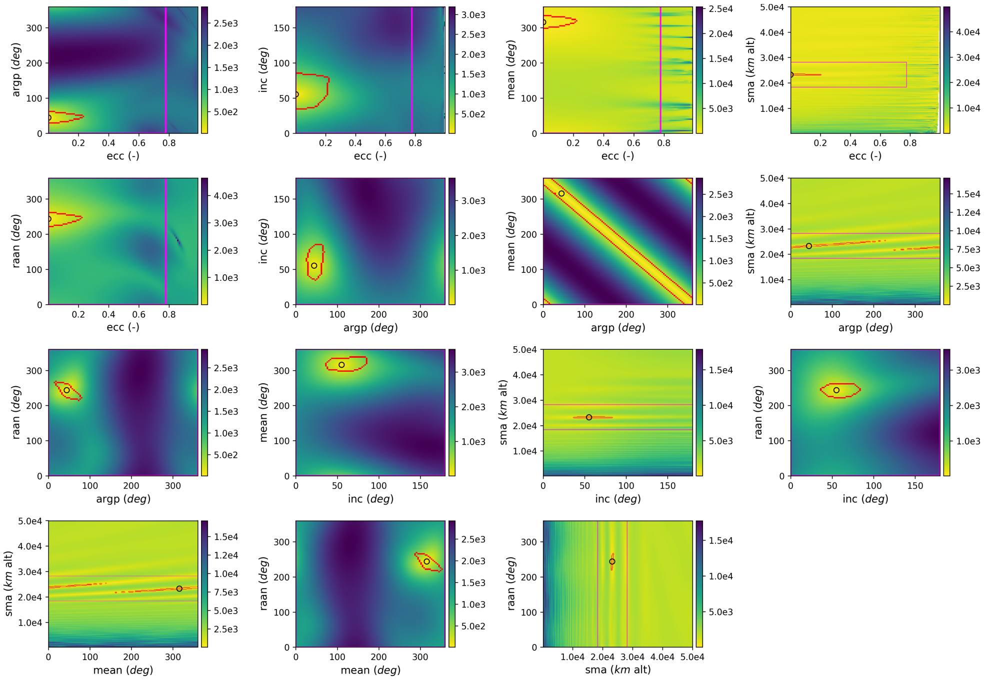

(a) Keplerian elements

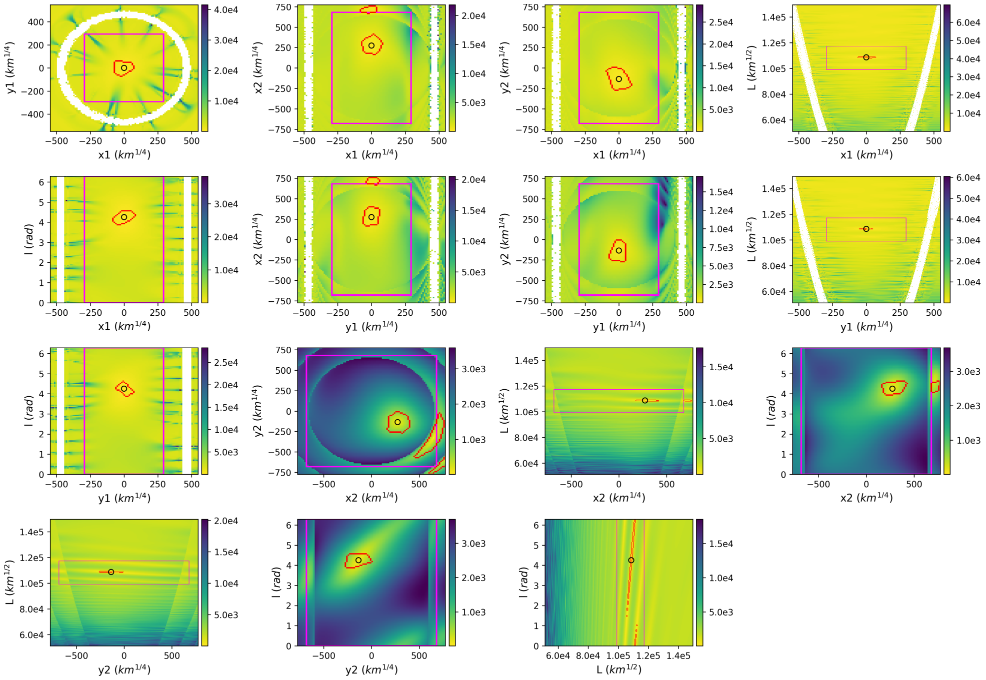

(b) Poincaé elements

Fig. 2: FDOA cost function evaluated over two-dimensional slices of the Poincaré state-space around truth for a simulated Galileo GNSS satellite (NORAD 40889, Section 3.3). Lower residual costs are shown in yellow with the true TLE state circled in black. The red borders denote states visible above the horizon at all measurements, and the pink borders denote altitude and eccentricity constraints (Section 3.1.2).

### 3.1.2 Bounded Minimization

The optimization problem for state estimation defined in Eq. 11 is complicated by the high degree of non-linearity in the measurement residual cost function (see Fig. 1). Given possible concerns with evaluation of the numerical derivative, we opt to use a direct-search algorithm, in particular the Nelder-Mead downhill simplex algorithm[9].

While the angular components of a given state vector can suffer from phase wrapping, conveniently mitigated in Poincaré elements, the search space can be bounded (and normalized). In particular, we can bound the semi-major axis (either $a$ or $L$) between a minimum and maximum altitude of choice — e.g., between 200m and 50,000km altitude, or narrower altitude bands. We also can bound the eccentricity given prior constraints or a reference altitude $a_{ref}$ such that the perigee and apogee $(a_{min}, a_{max})$ do not violate certain bounds.

$$e_{max} = \min\left\{1 - \frac{a_{min}}{a_{ref}} \quad ; \quad \frac{a_{max}}{a_{ref}} - 1\right\} \tag{16}$$

If the semi-major axis is restricted to a narrow band, $e_{max}$ may still be evaluated using a wider apogee/perigee pair to enable exploration of highly eccentric orbits. It is assumed that the $e_{max}$ limit is a sufficiently extreme upper bound on the true eccentricity when setting $a_{ref}$ to the hypothesized semi-major axis prior to minimization. It should be noted that this $e_{max}$ bound is defined using a fixed reference altitude to avoid a dependency between the searchable state space and the current state vector during minimization.

Fig.s 1 and 2 above illustrate altitude and eccentricity bounds using the known TLE as the reference trajectory. During minimization, several initial guesses at various reference altitudes can be solved in parallel.

In Keplerian space only these two elements are constrained and half of the terms suffer from phase wrapping $(M, \omega, \Omega)$. However, in Poincaré space both $x_1$ and $y_1$ are bounded between $\pm\sqrt{2L_{max}(1-\sqrt{1-e_{max}^2})}$, and $x_2$ and $y_2$ are bounded between $\pm\sqrt{4L_{max}}$. While the eccentricity constraint does bound the minimum radius of the $[x_2, y_2]$ vector, it is more convenient to let the bound on $\{x_1, y_1\}$ restrict the minimum values $\{x_2, y_2\}$ can take through their shared terms. Thus, the Poincaré element set only the suffers phase wrapping concerns in $\lambda$ and all other elements are constrained through $a$ and $e$.

Upon constraining the orbital elements, the explorable state-space can be normalized onto $[0, 1]$. To account for phase wrapping in $\lambda$, we normalize $[0, 2\pi] \rightarrow [0, 1]$, and permit exploration over the domain $[-0.5, 1.5]$.

### 3.1.3 Basin-Hopping

The simplex algorithm we use to perform minimization is unable to guarantee that a convergent solution is the global minima, especially under the significant range ambiguities in the TDOA. We therefore employ a stochastic basin-hopping algorithm which iteratively performs minimization and random state permutation[18, 11]. The step size is adaptively updated from an initial value based on probabilistic step acceptance tests to tractably explore the residual space. Similar to how the search space can be constrained in the local minimization problem, the acceptance test can also be controlled in the global minimization problem, enabling the step to be forcibly accepted or rejected. We leverage this capability to improve convergence as discussed in Section 3.2.1. We implemented the basin-hopping algorithm provided in SciPy; the number of iterations for the basin-hopping and minimization steps are set empirically to achieve accurate results in an acceptable run-time.

## 3.2 Sequential Algorithm

The IOD state estimate from Equation 11 cannot be solved for directly due to the substantial non-linearities introduced by the range ambiguity and lack of an informative prior. Attempting to apply the basin-hopping algorithm as-is will either take an intractable amount of run-time to solve or will fail outright. We instead consider a sequence of optimization problems, as shown in Fig. 3, to gradually accumulate information and constrain the problem.

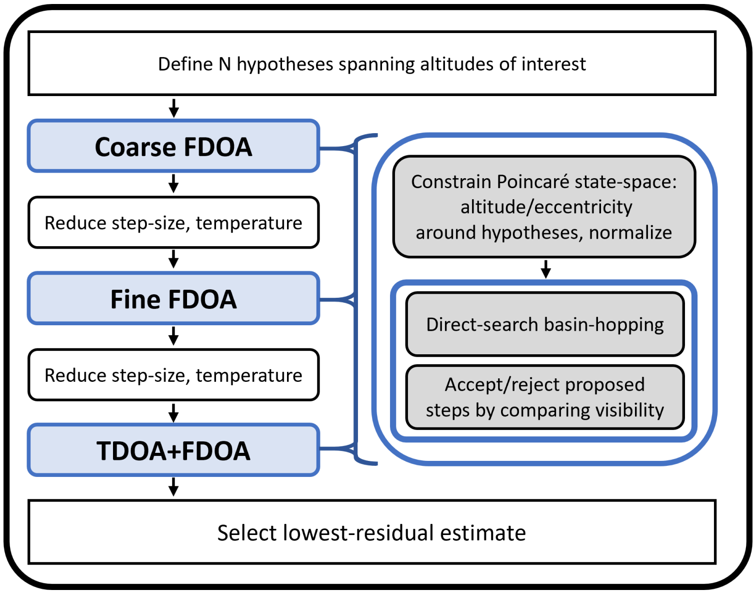

Fig. 3: Flowchart describing our initial orbit determination process.

### 3.2.1 Global FDOA optimization

There are several local minima in the FDOA residual cost function, mainly distributed as a function of the semi-major axis. If we apply bounds on these variables in the Poincaré element space, and solve in parallel for several narrow altitude "bands", the cost space can be heavily simplified. As the basin-hopping algorithm will readily propose a random state for subsequent steps, the other orbital elements for our initial guesses may be arbitrarily set to zero.

Table 1: Hypothesis reference trajectories used to begin the global FDOA optimization process. All other Keplerian orbital elements are set to zero.

| Minimum Altitude (km) | Maximum Altitude (km) | Range of Semimajor Axis Bounds (km) |
|---|---|---|
| 200 | 100 | 50 |
| 1,000 | 2,000 | 100 |
| 2,000 | 10,000 | 1,000 |
| 10,000 | 50,000 | 10,000 |

Only a small fraction of the state-space produces trajectories visible to all observers over the measurement set, i.e. producing transmitter positions which are above the horizon relative to each observer at appropriate measurement epochs. A straightforward approach would be to bound the search space to this domain, but we do not know this subspace a-priori. We can steer the global solver to the visible domain by evaluating a sum $J_\phi$ of the topocentric elevation angles $\phi$ from the receivers to the transmitting satellite over the measurement set, and evaluating the sum whenever the basin-hopping algorithm proposes a new perturbed state.

$$J_\phi(\mathbf{x}_{sv}(t_0^*)) = \sum_{i=1}^{N}\sum_{rx_j}\left(90^\circ - \phi(\mathrm{SGP4}(\mathbf{x}_{sv}(t_*),t_*,t_i) - \mathbf{x}^i_{rx_j})\right)^2 \tag{17}$$

If the previous minimization solution is within the visible domain (e.g., $\phi(\mathbf{x}^i_{sv} - \mathbf{x}^i_{rx_j}) \geq 0^\circ \ \forall i, j$), we will apply the standard Metropolis acceptance test if the proposed step remains in the visible domain and otherwise reject the step. If the previous solution is not in the visible domain, we will only accept proposed steps which reduce the visiblity cost function $J_\phi$. For the Metropolis acceptance test, the temperature is informed by an initial evaluation of the measurement residual cost function.

If the final solution within an altitude band after a given number of basin-hopping iterations is not within the visible domain, we will discard the hypothesis from further analysis. Otherwise, we will use the final state estimate as the initial hypothesis reference state for the next stage of the algorithm.

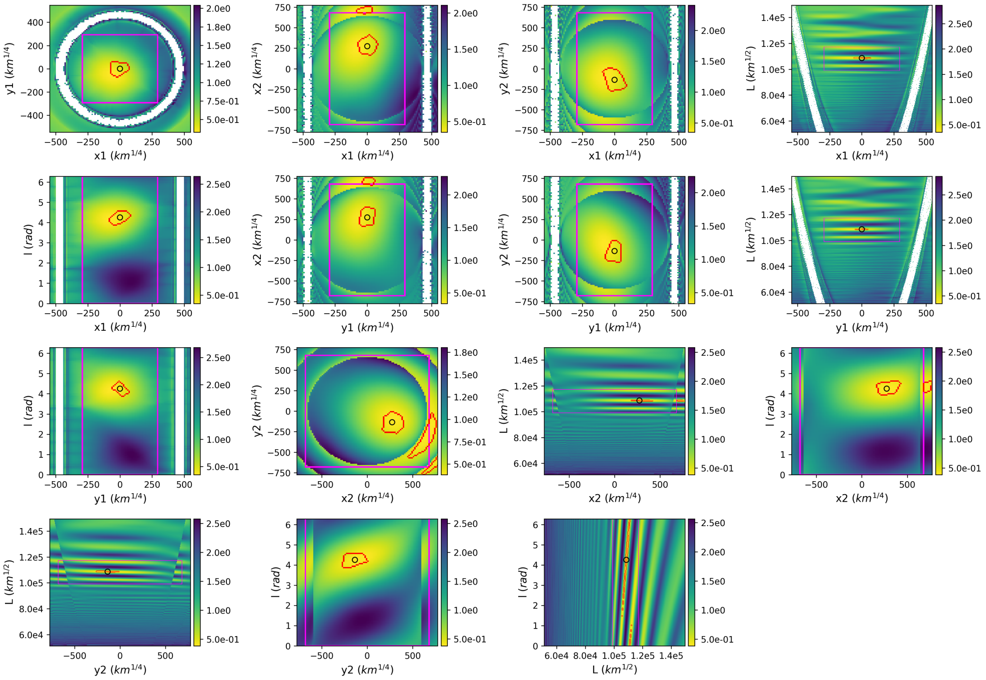

Fig. 4: Elevation-angle residual cost function $J_\phi$ evaluated over two-dimensional slices of the Poincaré state-space around truth for a simulated Galileo GNSS satellite (NORAD 40889, Section 3.3). Lower residual costs are shown in yellow with the true TLE state circled in black. The red borders denote states visible above the horizon at all measurements, and the pink borders denote altitude and eccentricity constraints (Section 3.1.2).

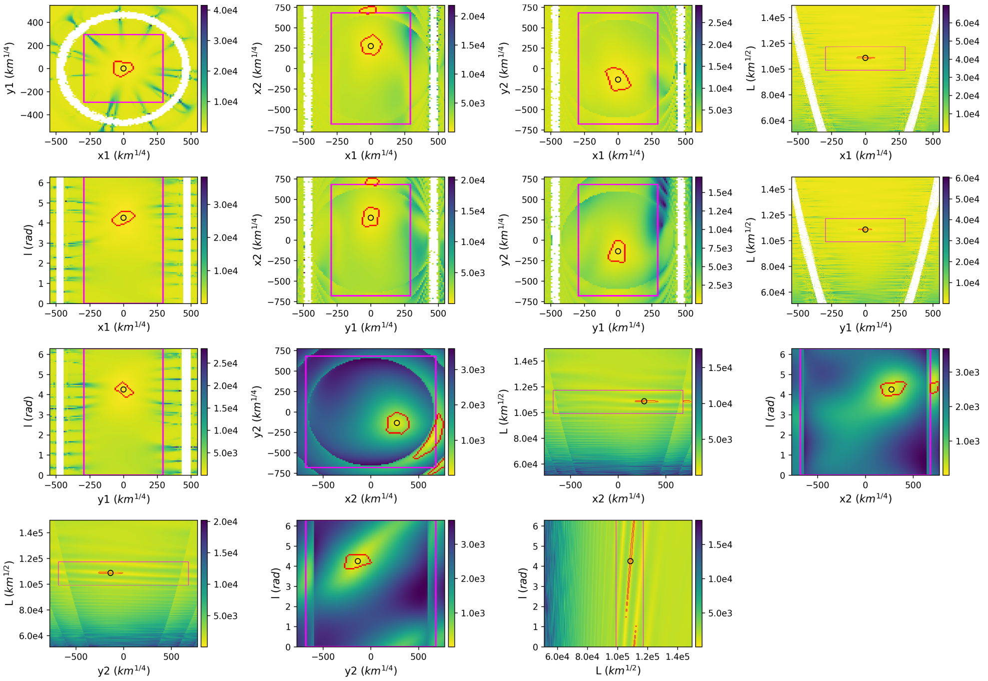

(a) Full state-space. Red borders denote states visible above the horizon at all measurements, pink borders denote altitude and eccentricity constraints.

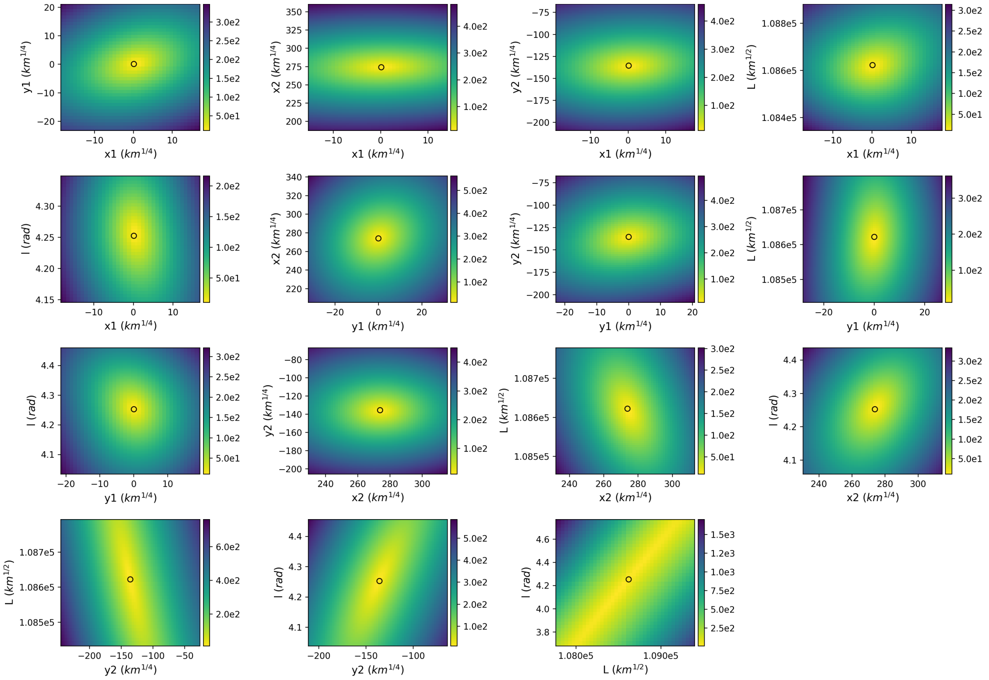

(b) Zoomed-in view.

Fig. 5: FDOA cost functions evaluated over two-dimensional slices of the Poincaré state-space around truth for a simulated Galileo GNSS satellite (NORAD 40889, Section 3.3). Lower residual costs are shown in yellow with the true TLE state circled in black.

### 3.2.2 Local FDOA optimization

Once we have identified an initial set of global solutions, we restrict the search space of each hypothesis to the visible domain around the reference state using the aforementioned elevation-angle acceptance test. The temperature and initial step-size for the basin-hopping algorithm and minimization algorithm are dramatically reduced, allowing for significantly improved convergence in some cases.

### 3.2.3 Local TDOA+FDOA optimization

The second stage of our algorithm produces a state which may not be sufficient to disambiguate the TDOA data, but which is close enough to enable basin-hopping to converge in a reasonable amount of time. Minimization is performed the same as above, but using all TDOA and FDOA measurement data as defined in Eq. 11. The acceptance test temperature is adjusted for the corresponding increase in the cost function from the new data, and the step size is once again reduced. If multiple hypotheses have survived to this point, the final IOD state estimate is determined to be the one with the lowest post-fit measurement residual.

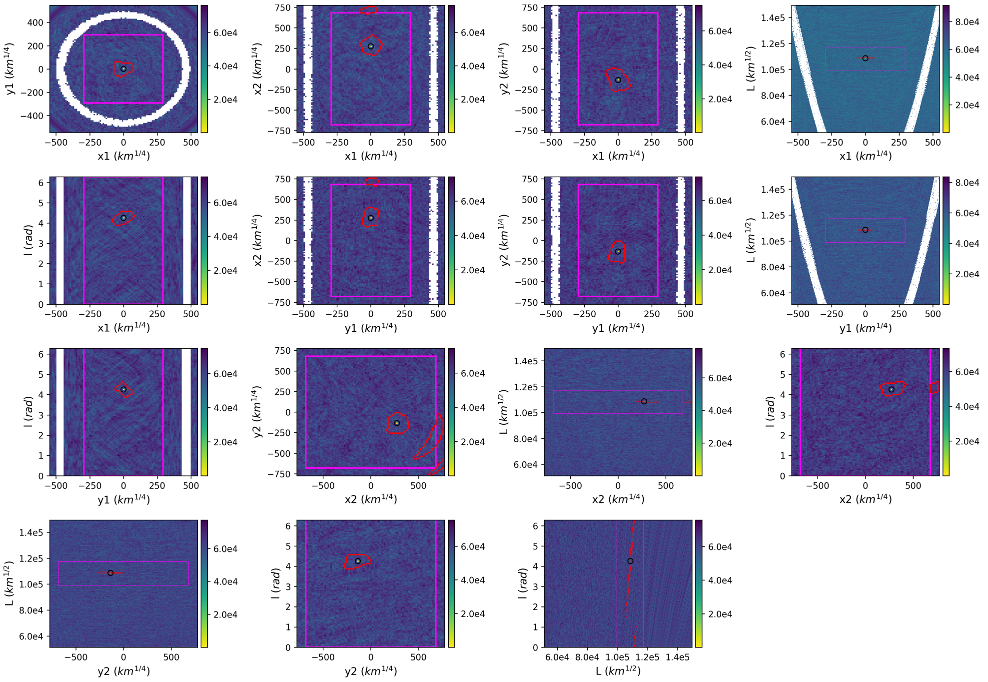

(a) Full state-space. Red borders denote states visible above the horizon at all measurements, pink borders denote altitude and eccentricity constraints.

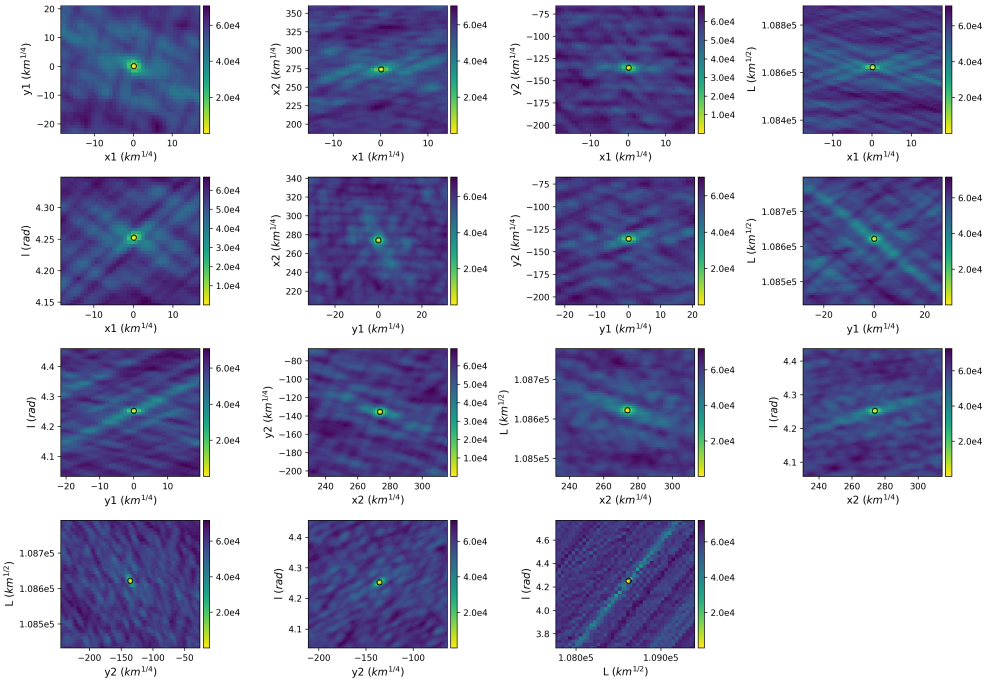

(b) Zoomed-in view.

Fig. 6: TDOA+FDOA cost functions evaluated over two-dimensional slices of the Poincaré state-space around truth for a simulated Galileo GNSS satellite (NORAD 40889, Section 3.3). Lower residual costs are shown in yellow with the true TLE state circled in black.

### 3.3 Test Data

To test the flexibility of our approach, we simulate a diverse set of space objects inspired by Riel et al[12], capturing a wide range of altitudes, eccentricities, and inclinations. We simulate pseudo-range and Doppler measurements from a globally distributed sensor network for a 24 hour period from April 12-13, 2024. As the list includes objects at vastly different altitudes, the measurement cadence is adjusted to be longer for higher-altitude orbits as done in operational practice, and for consistency a subset of 100 measurement samples (50 TDOA and 50 FDOA) is selected for each object. We also simulate each scenario as having an normally distributed standard deviation of 10m in range and 10Hz in frequency, a uniformly distributed satellite clock bias up to 1ms, and a pseudo-range ambiguity of 1ms. For the simulated data in this work, environmental factors such as ionospheric delay are ignored, and the position and clock biases of the observers are known.

To validate our results on the 22 simulated objects covered in this work, we consider 20 real GNSS satellites using real 30-second observation data provided through NASA's Crustal Dynamics Data Information System (CDDIS) [10, 3]. Of these real satellites, 16 belong to the GPS constellation in Medium Earth Orbit (MEO), 3 belong to the QZSS constellation in Geosynchronous Earth Orbit (GSO), and 1 belongs to the QZSS constellation in Geostationary Earth Orbit (GEO). A 1ms ambiguity in manually introduced to this data, and the sensor network and observation period are equivalent to the simulated tests.

The sensor network used in this work consists of 20 random International GNSS Service (IGS) Network stations providing RINEX V3 format observation data with both pseudorange and Doppler measurements. The daily 30-second observation data provides many more samples than necessary to this work, and we therefore considered a smaller sub-sample to work with. We isolated the L1:CA data and downsampled to 20-minute observations at regular epochs, and then removed samples below the median SNR for each station.

Table 2: Simulated objects considered in validating our algorithm.

| NORAD | Semimajor Axis (km alt.) | Eccentricity | Inclination (deg) |
|---|---|---|---|
| **25544** | 416.37 | 0.0005 | 51.64 |
| **36508** | 719.42 | 0.0005 | 92.03 |
| **27386** | 763.34 | 0.0001 | 98.28 |
| **5679** | 944.44 | 0.0010 | 70.00 |
| **24279** | 1082.22 | 0.0301 | 98.70 |
| **33105** | 1310.80 | 0.0008 | 66.04 |
| **41240** | 1337.73 | 0.0008 | 66.04 |
| **24827** | 2121.30 | 0.1072 | 63.30 |
| **22195** | 5783.75 | 0.0138 | 52.67 |
| **36501** | 6575.90 | 0.4843 | 49.63 |
| **19751** | 19125.57 | 0.0024 | 64.53 |
| **29670** | 19128.71 | 0.0021 | 64.70 |
| **37829** | 19129.93 | 0.0011 | 64.88 |
| **29671** | 19140.97 | 0.0021 | 64.71 |
| **43208** | 21528.03 | 0.0010 | 55.97 |
| **40889** | 23222.21 | 0.0005 | 55.25 |
| **41241** | 35785.32 | 0.0019 | 31.49 |
| **46114** | 35786.36 | 0.0002 | 0.00 |
| **28868** | 35786.59 | 0.0003 | 2.26 |
| **40549** | 35788.95 | 0.0036 | 50.69 |
| **3623** | 38871.56 | 0.0092 | 6.09 |
| **3674** | 40722.17 | 0.0179 | 11.56 |

Table 3: Real GNSS satellites considered in validating our algorithm.

| NORAD | Semimajor Axis (km alt.) | Eccentricity | Inclination (deg) |
|---|---|---|---|
| **39741** | 20181.38 | 0.0032 | 56.71 |
| **40534** | 20181.70 | 0.0087 | 53.37 |
| **55268** | 20181.77 | 0.0002 | 55.08 |
| **32711** | 20181.99 | 0.0185 | 54.45 |
| **24876** | 20182.04 | 0.0077 | 55.65 |
| **39533** | 20182.14 | 0.0072 | 53.60 |
| **29601** | 20182.23 | 0.0087 | 55.16 |
| **39166** | 20182.25 | 0.0124 | 55.17 |
| **41019** | 20182.33 | 0.0095 | 56.35 |
| **40105** | 20182.38 | 0.0025 | 54.90 |
| **27704** | 20182.50 | 0.0254 | 55.11 |
| **28474** | 20182.52 | 0.0163 | 55.43 |
| **29486** | 20182.56 | 0.0104 | 54.68 |
| **38833** | 20182.75 | 0.0150 | 53.51 |
| **40294** | 20182.94 | 0.0051 | 56.37 |
| **43873** | 20183.15 | 0.0029 | 55.27 |
| **49336** | 35783.74 | 0.0752 | 35.81 |
| **42965** | 35786.63 | 0.0748 | 40.54 |
| **42738** | 35791.66 | 0.0742 | 40.68 |
| **42917** | 35786.14 | 0.0002 | 0.05 |

Table 4: IGS Network stations used in this study (see Fig. 7).

| IGS Station Name | Monument/Receiver Number | ISO Country Code |
|---|---|---|
| **ANTF** | 00 | CHL |
| **BAIE** | 00 | CAN |
| **CHPG** | 00 | BRA |
| **CPVG** | 00 | CPV |
| **CUIB** | 00 | BRA |
| **FRDN** | 00 | CAN |
| **HERT** | 00 | GBR |
| **ISHI** | 00 | JPN |
| **JFNG** | 00 | CHN |
| **KARR** | 00 | AUS |
| **METG** | 00 | FIN |
| **MOBS** | 00 | AUS |
| **PICL** | 00 | CAN |
| **POHN** | 00 | FSM |
| **RGDG** | 00 | ARG |
| **RIGA** | 00 | LVA |
| **SOFI** | 00 | BGR |
| **SOLO** | 00 | SLB |
| **TWTF** | 00 | TWN |
| **VOIM** | 00 | MDG |

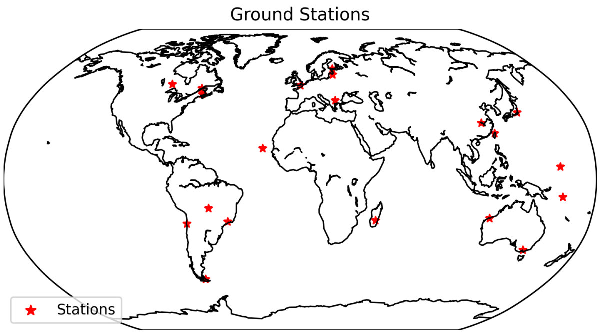

Fig. 7: IGS Network stations used in this study (see Table 4).

## 4. RESULTS

### 4.1 Statistics of Interest

To evaluate whether the final IOD state estimate is sufficient to disambiguate the measurements for precision OD, we compare the geometric TDOAs of the estimate $\hat{\mathbf{x}}_{sv}^*$ to those produced by the known TLE state $\mathbf{x}_{TLE}^*$ at the epochs / receivers of the measurement set. If this statistic falls within half the ambiguity ($\max \varepsilon_{TDOA} < cT_f/2$) then the IOD state estimate is considered to be successful.

$$\max \varepsilon_{TDOA} = \max_{i=1:N} \left|\tilde{\Delta}_T^i(\mathbf{x}_{TLE}^*) - \tilde{\Delta}_T^i(\hat{\mathbf{x}}_{sv}^*)\right| \tag{18}$$

While the above statistic can be used for determining whether we can disambiguate the data, it does not describe how well the state estimate corresponds to the true TLE over the entire trajectory, especially as the number of measurements decreases. We thus also consider the RMS position error of the state vector, taken for 100 evenly-spaced samples over one complete orbit. This statistic does not directly relate to the disambiguation problem, but can inform whether the IOD estimate will be good for seeding a precision OD solver, such as a linear Kalman filter.

$$\mathrm{RMS}\varepsilon_{\mathbf{x}} = \sqrt{\frac{1}{N}\sum_{i=1}^{N} \|\mathbf{x}_{TLE}^* - \hat{\mathbf{x}}_{sv}^*\|_2^2} \tag{19}$$

### 4.2 Simulated Data

For the simulated scenarios, the only situation where IOD failed was for the Geostationary objects. All other objects fell within the $\max \varepsilon_{TDOA} < cT_f/2$ tolerance (Fig. 8) and had a low one-orbit error $\mathrm{RMS}\varepsilon_{\mathbf{x}}$ (Fig. 9). This is true for objects at LEO, GSO, and Graveyard-orbit altitudes, as well as for highly eccentric and polar orbits.

In the failure cases, the FDOA went to zero for all states within the Geostationary belt, i.e., the mean longitude solution is undefined. This appears to leave too wide a space for the basin-hopping algorithm to reasonably explore after introducing TDOA measurements. In the other cases, the FDOA could be uniquely determined, but the local minimum was too broad for reliable disambiguation using FDOA data alone (see Fig. 8b, in particular the dark blue upward-triangle representing a GSO objects).

Even for cases where the FDOA estimate was within the disambiguation tolerance, the error is high enough to suggest that an FDOA-only approach would not be sufficient in general. Inspecting the RMS statistics, we see that for cases where the FDOA estimate appeared to be sufficient, the final state estimate had significant error throughout the orbit, which could be detrimental for subsequent precision OD — e.g., prior error being too high to accurately linearize the system (see Fig. 9b, in particular the squares representing GNSS objects).

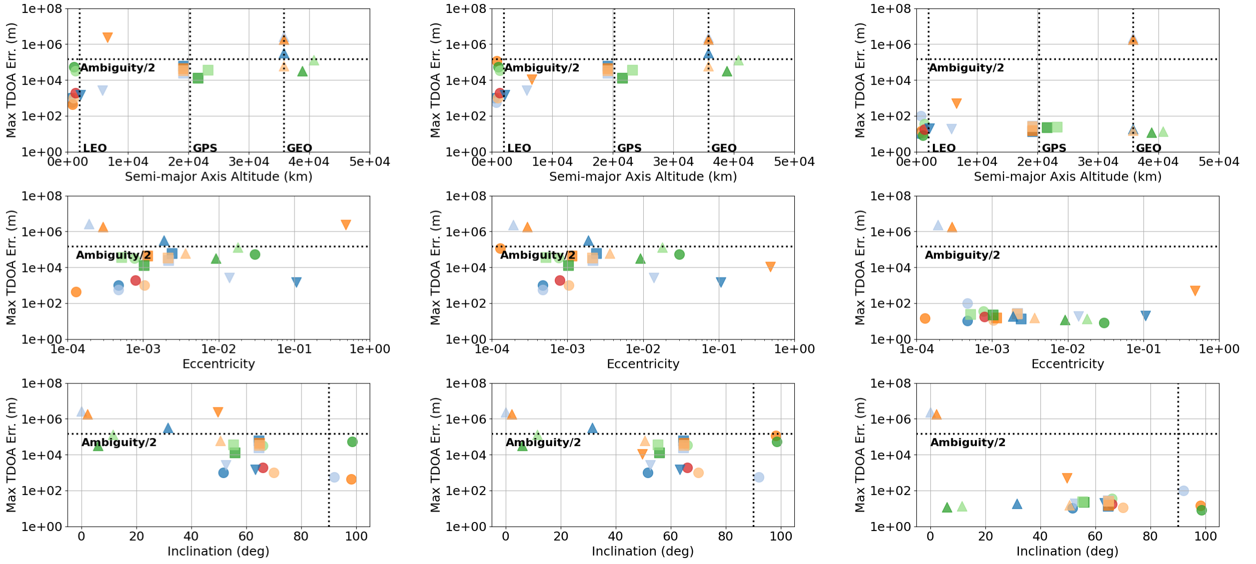

(a) Coarse FDOA estimate

(b) Fine FDOA estimate

(c) TDOA+FDOA estimate

Fig. 8: Simulated data analysis. Maximum TDOA error between true TLE and state estimate across observations. Markers denote the state estimate for each unique space object.

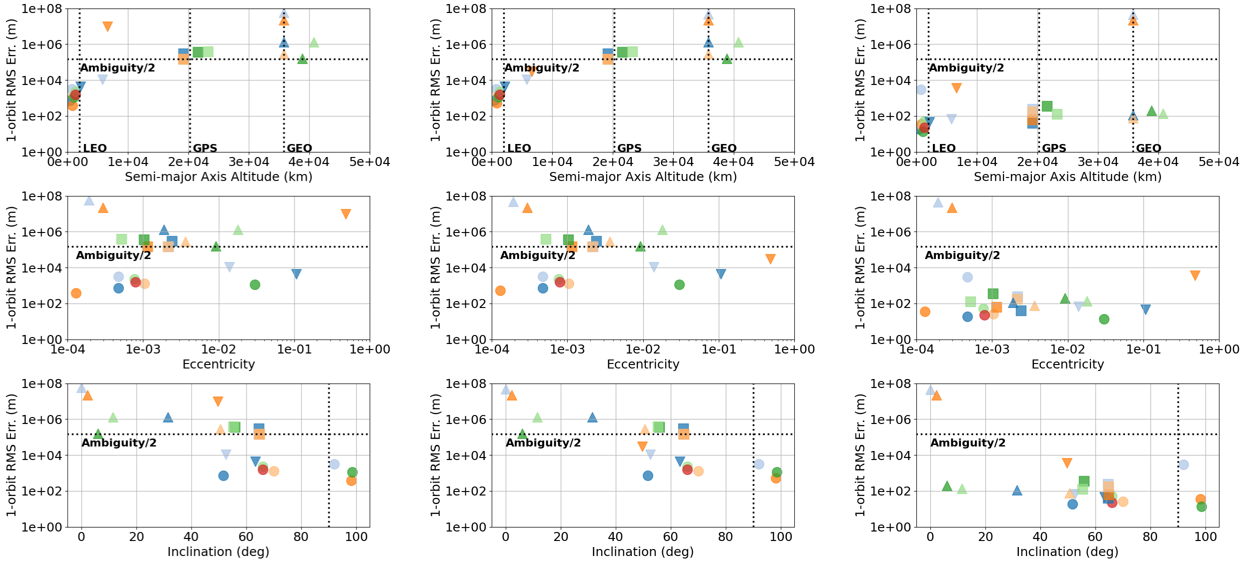

(a) Coarse FDOA estimate

(b) Fine FDOA estimate

(c) TDOA+FDOA estimate

Fig. 9: Simulated data analysis. One-orbit RMS position error between true TLE and state estimate. Markers denote the state estimate for each unique space object.

### 4.3 Real Data

For the real data scenarios, IOD again only failed in the Geostationary case as expected. The other MEO and GSO satellites were successfully estimated. While the max $\varepsilon_{TDOA} < cT_f/2$ tolerance again appears to be sufficient after FDOA-only analysis (Fig. 10b), the one-orbit RMS metric suggests that the complete trajectories may have too high an error for use as priors (Fig. 11b) requiring subsequent basin-hopping using TDOA measurements.

Errors in the real data scenarios are noticeably higher than present in the simulated data analysis. This may be due to a variety of environmental effects not considered in the current measurement model which should be included in future work. However, IOD estimation is merely intended to seed more extensive precision OD algorithms, and so this is not a concern for the current work.

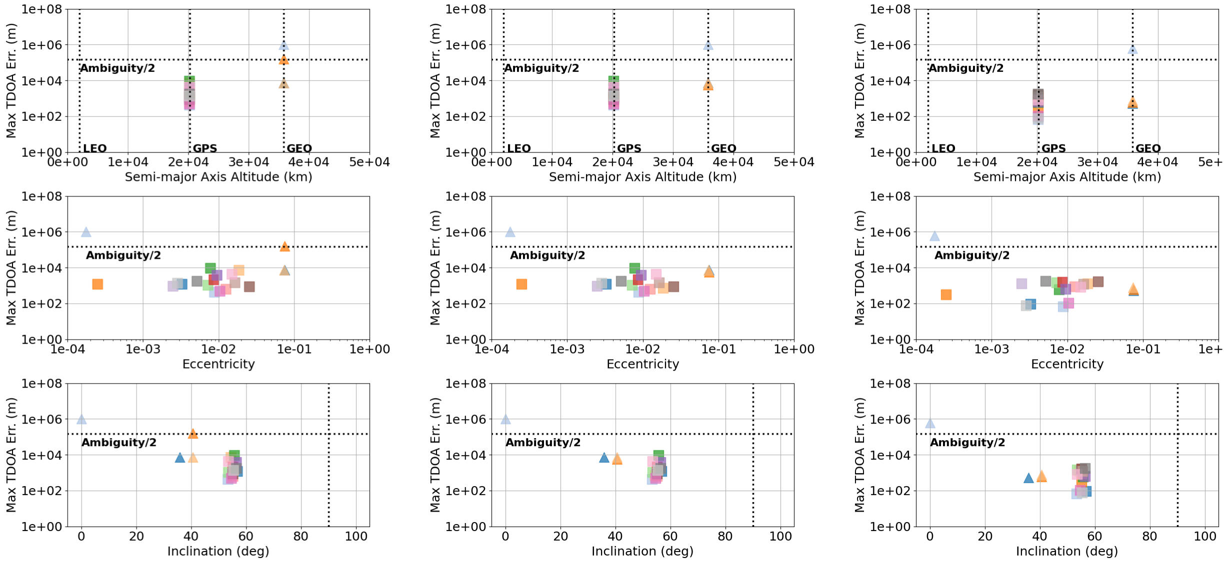

(a) Coarse FDOA estimate (b) Fine FDOA estimate (c) TDOA+FDOA estimate

Fig. 10: Real data analysis. Maximum TDOA error between true TLE and state estimate across observations. Markers denote the state estimate for each unique space object.

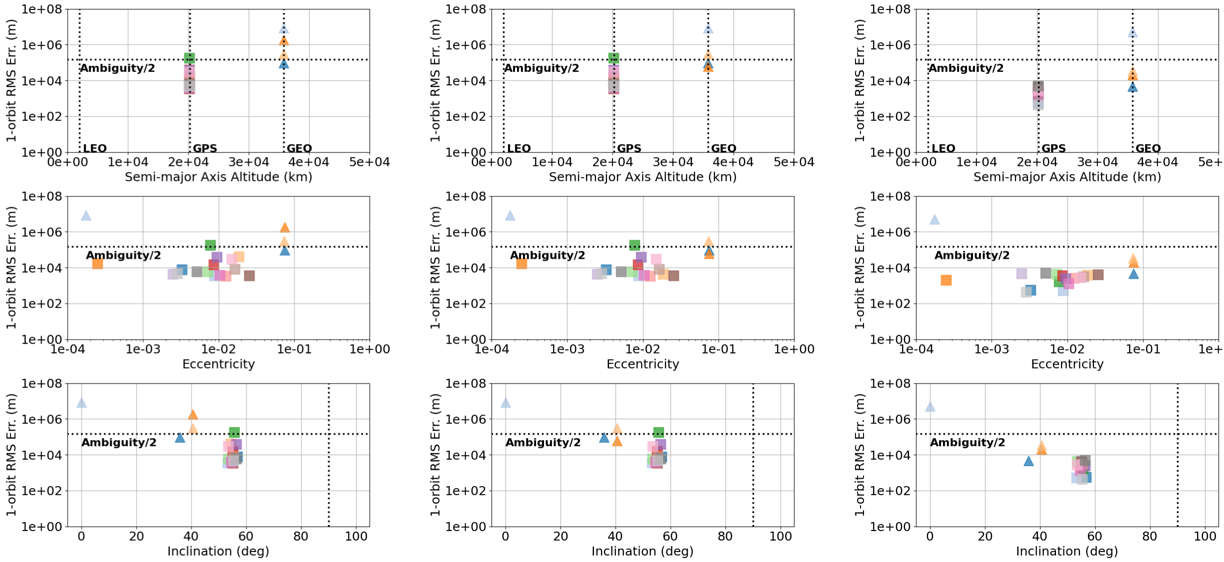

(a) Coarse FDOA estimate (b) Fine FDOA estimate (c) TDOA+FDOA estimate

Fig. 11: Real data analysis. One-orbit RMS position error between true TLE and state estimate. Markers denote the state estimate for each unique space object.

## 5. CONCLUSIONS

This work presents an IOD algorithm for determining the orbital state of a space-based transmitter from passive RF data in the presence of phase ambiguities. We map pseudo-range and Doppler frequency shift observables to TDOA and FDOA measurements in order perform coarse state estimation prior to solving for the unknown transmitter clock bias and drift.

By posing the problem in terms of sequential direct-search basin-hopping minimization in Poincaré element space, we are able to successfully detect a wide range of simulated objects (including LEO and highly eccentric objects) and real GNSS satellites (including GSO satellites) without making any substantial prior assumptions about the transmitter states. This may enable detection and tracking of arbitrary active satellites during daylight hours and at long ranges (Geostationary orbits or higher), mitigating risks of custody loss, cross-tagging, and low-certainty conjunction assessment.

We have demonstrated the efficacy of the proposed algorithm on the simulated and real data by comparing the maximum post-fit residuals of the state estimate to the signal ambiguity, demonstrating that the signals can be disambiguate for subsequent precision OD. We also demonstrated that the algorithm produces estimates with low RMS position error relative to truth across full orbit trajectories, supporting use as a prior for precision OD.

Geostationary satellites in the both the simulated and real data were the only objects observed for which the proposed algorithm failed, likely due to undefined solution for the mean longitude along the GEO belt in the FDOA cost space. In future work, if the initial FDOA estimate yields a near-GEO state, we are interested in launching several parallel solvers using TDOA measurements initialized at hypotheses spanning the mean longitude. We also are interested in exploring the minimum number of measurements necessary for successful estimation across the various orbital configurations, and validating our simulations on more extensive real data sets.

## 6. ACKNOWLEDGMENTS

The data used in this study were acquired as part of NASA's Earth Science Data Systems and archived and distributed by the Crustal Dynamics Data Information System (CDDIS) [10, 3]. The authors would like to thank Matthew Graham for his help in reviewing this work.

## 7. REFERENCES

[1] Daniel Casanova, Alexis Petit, and Anne Lemaître. Long-term evolution of space debris under the j 2 effect, the solar radiation pressure and the solar and lunar perturbations. *Celestial Mechanics and Dynamical Astronomy*, 123(2):223–238, 2015. `doi:10.1007/s10569-015-9644-1`.

[2] Luca Collettini, Lorenzo Frezza, Fabrizio Piergentili, Fabio Santoni, and Paolo Marzioli. Performance analysis of a time difference of arrival sensors network for leo satellites orbit determination. *Aerospace Science and Technology*, 142:108601, 2023. `doi:10.1016/j.ast.2023.108601`.

[3] Crustal Dynamics Data Information System (CDDIS DAAC). International gnss service, daily 30-second observation data. Available on-line [`http://cddis.gsfc.nasa.gov/Data_and_Derived_Products/GNSS/daily_gnss_o.html`] from NASA EOSDIS CDDIS DAAC, Greenbelt, MD, U.S.A. Accessed May 13, 2024. Subset obtained: time period: 2023-04-12 to 2023-04-13, 2024. `doi:10.5067/GNSS/gnss_daily_o_001`.

[4] Kohei Fujimoto, Daniel J Scheeres, and K Terry Alfriend. Analytical nonlinear propagation of uncertainty in the two-body problem. *Journal of Guidance, Control, and Dynamics*, 35(2):497–509, 2012. `doi:10.2514/1.54385`.

[5] Jeroen Geeraert, Jay W McMahon, and Brandon A Jones. Orbit determination observability of the dual-satellite geolocation system with tdoa and fdoa. In *AIAA/AAS Astrodynamics Specialist Conference*, page 5367, 2016. `doi:10.2514/6.2016-5367`.

[6] E Griggs, M Schierholtz, I Hussein, M Bolden, K Charles, and H Borowski. Probabilistic initial orbit determination and object tracking in cislunar space using passive radio frequency sensors. In *Proceedings of the Advanced Maui Optical and Space Surveillance (AMOS) Technologies Conference*, page 19, 2023.

[7] Sharbel Kozhaya, Haitham Kanj, and Zaher M Kassas. Multi-constellation blind beacon estimation, doppler tracking, and opportunistic positioning with oneweb, starlink, iridium next, and orbcomm leo satellites. In

*2023 IEEE/ION Position, Location and Navigation Symposium (PLANS)*, pages 1184–1195. IEEE, 2023. `doi:10.1109/PLANS53410.2023.10139969`.

[8] Elvis Lacruz, Daniel Casanova, and Alberto Abad. Estimation of a reliability range for the area-to-mass ratio of orbiters at the geostationary ring. *Acta Astronautica*, 166:104–112, 2020. `doi:10.1016/j.actaastro.2019.09.039`.

[9] John A Nelder and Roger Mead. A simplex method for function minimization. *The computer journal*, 7(4):308–313, 1965. `doi:10.1093/comjnl/7.4.308`.

[10] Carey E. Noll. The crustal dynamics data information system: A resource to support scientific analysis using space geodesy. *Advances in Space Research*, 45(512):1421–1440, 2010. `doi:10.1016/j.asr.2010.01.018`.

[11] Brian Olson, Irina Hashmi, Kevin Molloy, and Amarda Shehu. Basin hopping as a general and versatile optimization framework for the characterization of biological macromolecules. *Advances in Artificial Intelligence*, 2012(1):674832, 2012. `doi:10.1155/2012/674832`.

[12] Thomas Riel, Andras Galffy, Georg Janisch, Daniel Wertjanz, Andreas Sinn, Christian Schwaer, and Georg Schitter. High performance motion control for optical satellite tracking systems. *Advances in Space Research*, 65(5):1333–1343, 2020. `doi:10.1016/j.asr.2019.11.039`.

[13] Simon Shuster, Andrew J Sinclair, and T Alan Lovell. Initial relative-orbit determination using heterogeneous tdoa. In *2017 IEEE Aerospace Conference*, pages 1–7. IEEE, 2017. `doi:10.1109/AERO.2017.7943779`.

[14] Andrew J Sinclair, Edwin GW Peters, Joseph TA Peterson, and Melrose Brown. Probabilistic initial orbit determination from radio frequency measurements using gaussian mixture. In *Proceedings of the Advanced Maui Optical and Space Surveillance (AMOS) Technologies Conference*, page 180, 2023.

[15] David A Vallado. *Fundamentals of astrodynamics and applications*, volume 4. Microcosm Press, 2013.

[16] David A Vallado, Paul Crawford, Richard Hujsak, and T S Kelso. Revisiting spacetrack report #3. In *AIAA/AAS Astrodynamics Specialist Conference*, Aug 21-24 2006. `doi:10.2514/6.2006-6753`.

[17] Kullen Waggoner, David Curtis, and Bryan Little. Analysis of tdoa/fdoa state estimation accuracy of cislunar objects for space situational awareness. In *2023 IEEE Aerospace Conference*, pages 1–11. IEEE, 2023. `doi:10.1109/AERO55745.2023.10115697`.

[18] David J Wales and Jonathan PK Doye. Global optimization by basin-hopping and the lowest energy structures of lennard-jones clusters containing up to 110 atoms. *The Journal of Physical Chemistry A*, 101(28):5111–5116, 1997. `doi:10.1021/jp970984n`.